Publication Year	2022
Acceptance in OA@INAF	2022-11-03T09:52:19Z
Title	Collision of protostellar jets in the star-forming region IC 1396N. Analysis of knot proper motions
Authors	López, Rosario; Estalella, Robert; BELTRAN SOROLLA, MARIA TERESA; MASSI, Fabrizio; Acosta-Pulido, José A.; et al.
DOI	10.1051/0004-6361/202243380
Handle	http://hdl.handle.net/20.500.12386/32709
Journal	ASTRONOMY & ASTROPHYSICS
Number	661

A&A 661, A106 (2022)
https://doi.org/10.1051/0004-6361/202243380
© ESO 2022

Astronomy & Astrophysics

Collision of protostellar jets in the star-forming region IC 1396N

Analysis of knot proper motions★

Rosario López[1], Robert Estalella[1], Maria T. Beltrán[2], Fabrizio Massi[2], José A. Acosta-Pulido[3], and Josep M. Girart[4,5]

[1] Departament de Física Quàntica i Astrofísica, Institut de Ciències del Cosmos, Universitat de Barcelona, IEEC-UB, Martí i Franquès, 1, 08028 Barcelona, Spain
e-mail: rosario@fqa.ub.edu
[2] INAF – Osservatorio Astrofisico di Arcetri, Largo E. Fermi 5, 50125 Firenze, Italy
[3] Instituto de Astrofísica de Canarias, Avenida Vía Láctea, 38205 La Laguna, Tenerife, Spain
[4] Institut de Ciències de l'Espai (ICE), CSIC, Carrer de Can Magrans, s/n, 08193, Cerdanyola del Vallès, Catalonia, Spain
[5] Institut d'Estudis Espacials de Catalunya (IEEC), 08034 Barcelona, Catalonia, Spain

Received 21 February 2022 / Accepted 21 March 2022

ABSTRACT

Context. The bright-rimmed cloud IC 1396N is believed to host one of the few known cases where two bipolar CO outflows driven by young stellar objects collide. The CO outflows are traced by chains of knots of H_2 emission, with enhanced emission at the position of the possible collision.
Aims. The aim of this work is to use the proper motions of the H_2 knots to confirm the collision scenario.
Methods. A second-epoch H_2 image was obtained, and the proper motions of the knots were determined with a time baseline of ∼11 yr. We also performed differential photometry on the images to check the flux variability of the knots.
Results. For each outflow (N and S), we classified the knots as pre-collision or post-collision. The axes of the pre-collision knots, the position of the possible collision point, and the axes of the post-collision knots were estimated. The difference between the proper motion direction of the post-collision knots and the position angle from the collision point was also calculated. For some of the knots, we obtained the 3D velocity using the radial velocity derived from H_2 spectra.
Conclusions. The velocity pattern of the H_2 knots in the area of interaction (post-collision knots) shows a deviation from that of the pre-collision knots, consistent with being a consequence of the interaction between the two outflows. This favours the interpretation of the IC 1396N outflows as a true collision between two protostellar jets instead of a projection effect.

Key words. Herbig-Haro objects – ISM: jets and outflows – ISM: individual objects: IC 1396N

1. Introduction

Jets and outflows are ubiquitous in star-forming regions, but cases of interaction between outflows are extremely rare. Indeed, only two cases of apparent collision between jets or outflows are known, the IC 1396N outflows (Beltrán et al. 2012) and BHR 71 (Zapata et al. 2018). In BHR 71, the red lobe and the blue lobe of two different CO outflows collide, and in the area of interaction there is an increase in CO emission and a broadening of the lines consistent with the collision scenario.

IC 1396N is a bright-rimmed cloud (BRC38; Sugitani et al. 1991) located in the Cep OB2 association. We adopt an updated value for the distance to IC 1396N of 910 ± 49 pc, obtained from the catalogue of distances to molecular clouds of Zucker et al. (2020). IC 1396N shows a cometary structure elongated in the south–north direction, and is associated with an intermediate-mass star-forming region where a number of Herbig-Haro objects, H_2 jet-like features, CO molecular outflows, and millimetre compact sources have been reported (see Beltrán et al. 2009, for a thorough description of the region). Deep near-infrared (NIR) images through the 2.12 μm H_2 $\upsilon = 1$–0 S(1) line of IC 1396N carried out with the 3.58 m Telescopio Nazionale *Galileo* (TNG) by Beltrán et al. (2009) reveal a number of small-scale H_2 emission features spread all over the globule, which are resolved into several chains of knots, showing a jet-like morphology and possibly tracing different H_2 outflows.

Two well-collimated bipolar CO outflows (outflows N and S) toward the northern part of the globule were reported by Beltrán et al. (2012). In both outflows, the blueshifted and redshifted lobes emanate from sources traced by their dust continuum emission (source C for outflow N and source I for outflow S) located at their symmetry centre (see Fig. 1). Both CO outflows are associated with several chains of H_2 knots reported by Beltrán et al. (2009): the H_2 chains of knots D and F lie along the redshifted lobes of the N and S outflows, respectively, while the chain of C knots lie at the position where the CO-North and CO-South blueshifted outflow lobes overlap.

Beltrán et al. (2009, 2012) propose that the outflows N and S are colliding at the position of the C knots, explaining the strong H_2 emission of this chain of knots, although this is not the only possible explanation: for example, it could be a projection effect, with the two outflows being in different planes. However, the facts that the two outflows are almost in the plane of the sky (inclination $i < 10°$) and the powering sources are at the same systemic velocity ($V_{LSR} \simeq 0$ km s^{-1}) favour the collision scenario.

With the aim of shedding new light on whether the overlapping blueshifted lobes are only a projection effect or, on

★ Partially based on service observations (SW2015a35) made with the WHT telescope operated on the island of La Palma by the ING in the ORM of the IAC.

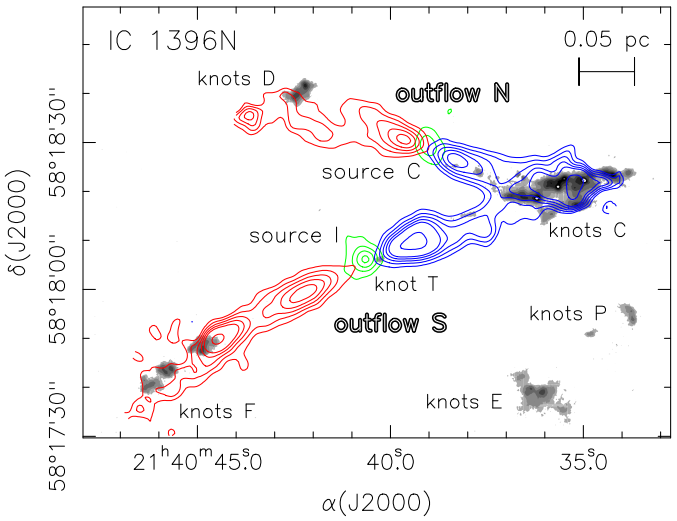

Fig. 1. CO outflows (red and blue contours), dust continuum emission (green contours), and H_2 emission (grey scale) from Beltrán et al. (2012). Source C traces the driving source of outflow N, while source I traces the driving source of outflow S.

the contrary, are tracing the collision of the two outflows, we decided to obtain the proper motions of the H_2 knots of IC 1396N northern outflows. Currently, proper motions of jet knots are used as an indirect tool for identifying the outflow driving source in regions with complex outflow activity: assuming that the knot motions are ballistic, the directions of their proper motion diverge from the location of the driving source. In the case of the IC 1396N northern outflows, if the superposition is only a projection effect, we would expect the pattern of tangential velocities to be the same for the C knots as for the other knots. On the other hand, if there is a true collision, we would expect the pattern of tangential velocities of the C knots to be modified by the collision. In order to derive the proper motions of the H_2 knots projected onto the outflow lobes, we obtained a second-epoch, deep H_2 υ = 1–0 S(1) image of IC 1396N. In addition, for some of the knots we were able to complement their tangential velocity with the line-of-sight velocity obtained from the spectroscopic H_2 υ = 1–0 S(1) observations of Massi et al. (2022).

In Sect. 2, we describe the observations and the derivation of the proper motions, in Sect. 3 we present the results obtained from our analysis of the pattern of proper motions obtained, and in Sect. 4 we discuss these results and outline our conclusions.

2. Observations and data reduction

The first epoch H_2 image of IC 1396N was obtained with the Near Infrared Camera Spectrometer (NICS) at the TNG during the observing run of the 2005 July 16 (all the details are given in Beltrán et al. 2009). The second epoch H_2 image was obtained on 2016 July 14 as a part of the Isaac Newton Group (ING) service-mode program with the Long-slit Intermediate Resolution Infrared Spectrograph (LIRIS) (Acosta-Pulido et al. 2003; Manchado et al. 2004) at the 4.2 m *Williams Herschel* Telescope (WHT) of the Observatorio del Roque de los Muchachos (ORM, La Palma, Spain). LIRIS is equipped with a Rockwell Hawaii 1024 × 1024 HgCdTe array detector. The spatial scale is 0.″25 pixel^{-1}, giving an image field of view (FOV) of 4.′27 × 4.′27. The observing strategy followed a three-point dithering pattern on-source interspersed with the same pattern for an off-source position of a field located ∼6 arcmin from the target. Three exposures of 50s were taken at each of the dither positions. The on-off cycle was repeated six times to complete a total on-source integration time of 2700 s. A typical value of the seeing was ∼0.″8.

Data were processed using the package *lirisdr* developed by the LIRIS team within the IRAF environment[1]. The reduction process included sky subtraction, flat-fielding, correction of geometrical distortion, and finally combination of frames using the common 'shift-and-add' technique. This final step consisted in dedithering and co-adding frames taken at different dither points to obtain a mosaic for each filter. The resulting mosaic covered a FOV of ∼5 arcmin^2.

2.1. Proper motions determination

Prior to evaluating knot proper motions, the two H_2 IC 1396 images were converted into a common reference system. The positions of 12 field stars common to the two frames were used to register the images. The *geomap* and *geotran* tasks of IRAF were applied to perform a linear transformation, with six free parameters that take into account translation, rotation, and magnification between different frames. After the transformation, the typical rms of the difference in position for the reference stars between the two images was ∼0.08 arcsec in both coordinates. The two images had the same spatial scale (0.25 arcsec pixel^{-1}), which was preserved by the transformation.

We defined boxes enclosing the emission of each of the H_2 knots that were identified in Beltrán et al. (2009). Then, the position offset in the x and y coordinates between the two epochs was calculated by cross-correlation. The uncertainty on the position of the correlation peak was estimated through the scatter of the correlation peak positions obtained from boxes differing from the nominal one by ±2 pixels. The error adopted for each coordinate for the offset between the two epochs was twice the uncertainty in the correlation peak position, added quadratically to the rms alignment error (see the description of the used method in Anglada et al. 2007).

2.2. Differential photometry

We carried out photometry on the H_2 images to check the variability of the line emission from the knots. In addition to our images, we also used an H_2 image obtained with NICS at the TNG on 2003 October 17 (Caratti o Garatti et al. 2006) and kindly provided by the authors. Continuum was not subtracted as the knots are barely affected by continuum emission and so as not to add additional errors. The three images were registered to a common reference frame as described in Sect. 2.1. We then performed aperture photometry on a sample of ∼200 common stars using the *phot* task of IRAF. The zero points were obtained as a weighted signal-to-noise (S/N) mean of the instrumental magnitudes, after excluding stars deviating more than 5σ to minimise the effects of variable stars. As we were only interested in differential photometry, we did not calibrate the zero points (the absolute knot photometry is already given in Beltrán et al. 2009).

The photometry of the knots was performed using the *polyphot* task of IRAF. For each knot, we defined a polygon on the 2005 image enclosing the emission down to a 5σ level and used the same polygons and sky annuli throughout the three images, as the image are on the same reference frame. We also

[1] IRAF is distributed by the National Optical Astronomy Observatories, which are operated by the Association of Universities for Research in Astronomy, Inc., under cooperative agreement with the National Science Foundation.

Table 1. Proper motions measured in IC 1396, tangential velocities for a distance of 910 pc, and 3D velocities for the knots whose radial velocity is known.

Knot	Id.[(d)]	μ_x (mas yr^{-1})	μ_y (mas yr^{-1})	v_x (km s^{-1})	v_y (km s^{-1})	v_t[(a)] (km s^{-1})	PA[(a)] (deg)	v_r[(b)] (km s^{-1})	$v_{\rm tot}$[(c)] (km s^{-1})	i[(c)] (deg)
D1	N-red	-4.23 ± 1.65	3.46 ± 1.25	-18.2 ± 7.1	14.9 ± 5.4	23.6 ± 6.5	51 ± 14	···	···	···
D2	N-red	-2.64 ± 1.42	0.90 ± 0.68	-11.4 ± 6.1	3.9 ± 2.9	12.1 ± 5.9	71 ± 14	···	···	···
C1	N-blue	8.68 ± 9.30	2.90 ± 2.54	37.5 ± 40.1	12.5 ± 10.9	39.5 ± 38.2	-72 ± 24	···	···	···
C3	N-blue	11.00 ± 4.70	-2.39 ± 2.51	47.4 ± 20.3	-10.3 ± 10.8	48.6 ± 19.9	-102 ± 14	···	···	···
C4	N-blue	-3.86 ± 3.26	-4.87 ± 5.28	-16.6 ± 14.1	-21.0 ± 22.8	26.8 ± 19.9	142 ± 39	···	···	···
C5	N-blue	2.27 ± 1.06	-2.28 ± 1.29	9.8 ± 4.6	-9.8 ± 5.6	13.9 ± 5.1	-135 ± 23	···	···	···
F1	S-red	-1.26 ± 0.92	2.02 ± 0.70	-5.4 ± 4.0	8.7 ± 3.0	10.3 ± 3.3	32 ± 20	9 ± 28	14 ± 19	41 ± 89
F2-3	S-red	-2.73 ± 1.09	-5.47 ± 1.22	-11.8 ± 4.7	-23.6 ± 5.3	26.4 ± 5.2	154 ± 11	-11 ± 28	29 ± 12	-23 ± 52
F4	S-red	-4.95 ± 2.87	0.84 ± 1.51	-21.4 ± 12.4	3.6 ± 6.5	21.7 ± 12.2	80 ± 17	-33 ± 28	39 ± 24	-57 ± 27
F5	S-red	-4.78 ± 3.26	0.64 ± 1.23	-20.6 ± 14.1	2.8 ± 5.3	20.8 ± 14.0	82 ± 14	4 ± 28	21 ± 15	11 ± 75
T	S-blue	6.15 ± 1.32	2.46 ± 0.90	26.5 ± 5.7	$10. \pm 3.9$	28.6 ± 5.5	-68 ± 8	···	···	···
C2	S-blue	9.66 ± 3.39	6.92 ± 2.86	41.7 ± 14.6	29.8 ± 12.4	51.3 ± 13.9	-54 ± 15	···	···	···
C6	N-post	-4.29 ± 2.68	3.83 ± 1.94	-18.5 ± 11.6	16.5 ± 8.4	24.8 ± 10.3	48 ± 24	-47 ± 23	53 ± 21	-62 ± 15
C7	N-post	7.06 ± 2.52	-3.28 ± 0.95	30.4 ± 10.9	-14.1 ± 4.1	33.6 ± 10.0	-115 ± 10	···	···	···
C9	N-post	-1.18 ± 1.43	0.49 ± 0.86	-5.1 ± 6.2	2.1 ± 3.7	5.5 ± 5.9	67 ± 43	···	···	···
C8	S-post	2.15 ± 1.58	1.91 ± 1.26	9.3 ± 6.8	8.2 ± 5.4	12.4 ± 6.3	-48 ± 28	-25 ± 23	28 ± 21	-64 ± 24
C10	S-post	6.45 ± 2.37	1.68 ± 0.90	27.8 ± 10.2	7.3 ± 3.9	28.7 ± 10.0	-75 ± 9	-43 ± 23	52 ± 20	-56 ± 17
C11	S-post	1.39 ± 1.25	-1.22 ± 1.03	6.0 ± 5.4	-5.3 ± 4.4	8.0 ± 5.0	-132 ± 35	···	···	···
C12	S-post	0.83 ± 0.76	0.83 ± 0.96	3.6 ± 3.3	3.6 ± 4.1	5.1 ± 3.7	-45 ± 41	···	···	···
C13	S-post	2.02 ± 0.80	1.84 ± 1.10	8.7 ± 3.4	8.0 ± 4.7	11.8 ± 4.1	-48 ± 20	···	···	···
C14	S-post	8.11 ± 2.07	-0.41 ± 0.75	35.0 ± 9.0	-1.8 ± 3.3	35.0 ± 8.9	-93 ± 6	-8 ± 23	36 ± 10	-13 ± 36
C15	S-post	3.77 ± 3.43	1.40 ± 1.32	16.2 ± 14.8	6.0 ± 5.7	17.3 ± 14.0	-70 ± 25	···	···	···
C16	S-post	2.86 ± 0.65	1.98 ± 0.63	12.3 ± 2.8	8.5 ± 2.7	15.0 ± 2.8	-55 ± 10	-10 ± 23	18 ± 13	-35 ± 62
C17	S-post	5.39 ± 2.51	1.62 ± 1.05	23.3 ± 10.8	7.0 ± 4.5	24.3 ± 10.4	-73 ± 13	···	···	···

Notes. [(a)]Tangential velocity and position angle, eastward from North. [(b)]Radial velocity from Massi et al. (2022); the errors quoted are the random plus systematic errors. [(c)]3D velocity; i is the inclination angle with respect to the plane of the sky, positive away from the observer. [(d)]Identification of the knot: outflow (N or S), and lobe, red, blue, or post-collision.

checked that the polygons were large enough to not be affected by the proper motions of the knots. The results are listed in Table A.1.

3. Results

3.1. Proper motions

Proper motions were determined for all the knots detected in the two images, except for knot C6, the morphology of which changed between the two epochs (see Fig. 2). The spurious proper motion determined for this knot will not be considered for the analysis.

The proper motions measured are shown in Table 1 and Figs. 3 and 4. In order to analyse the proper motions, we segregate the knots into different groups: outflow N pre-collision knots, from the east (redshifted) and west (blueshifted) lobes (N-red, N-blue), outflow S pre-collision knots, from the east (redshifted) and west (blueshifted) lobes (S-red, S-blue), and post-collision knots in the interaction area. The post-collision knots are tentatively identified as belonging to outflow N (N-post: knots C6, C7, C9) or to outflow S (S-post: C8 and C10 to C17). This identification will be justified later on, and is shown in Table 1.

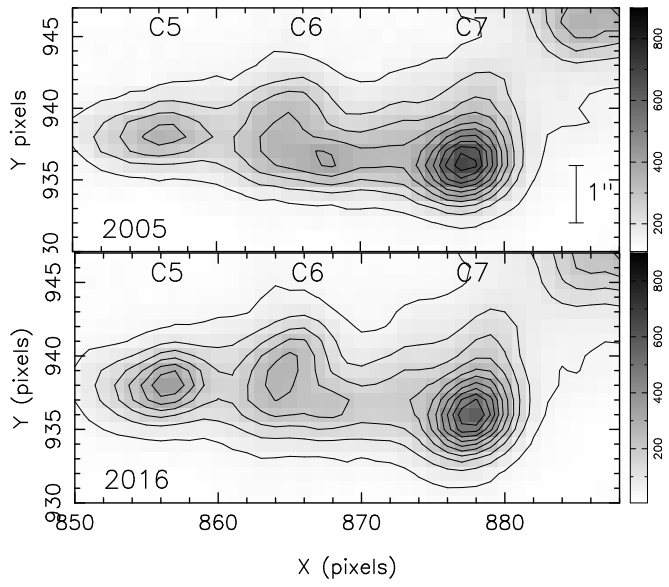

Fig. 2. H_2 emission of knots C5, C6, and C7 in the two epochs. The angular scale is indicated in the top panel. The morphology of knot C6 changes noticeably between the two epochs.

3.2. Direction of the outflows axes

3.2.1. Pre-collision knots

Following the nomenclature of Beltrán et al. (2012), outflow N is powered by source C (traced by dust continuum emission) with coordinates $\alpha(J2000) = 21^{\rm h}40^{\rm m}39\overset{\rm s}{.}04$, $\delta(J2000) = +58°18'29\overset{''}{.}8$. The knots D1 and D2 are moving eastward (CO red lobe), and C1, C3, C4, and C5 are moving westward (CO blue lobe), toward the area of interaction (see

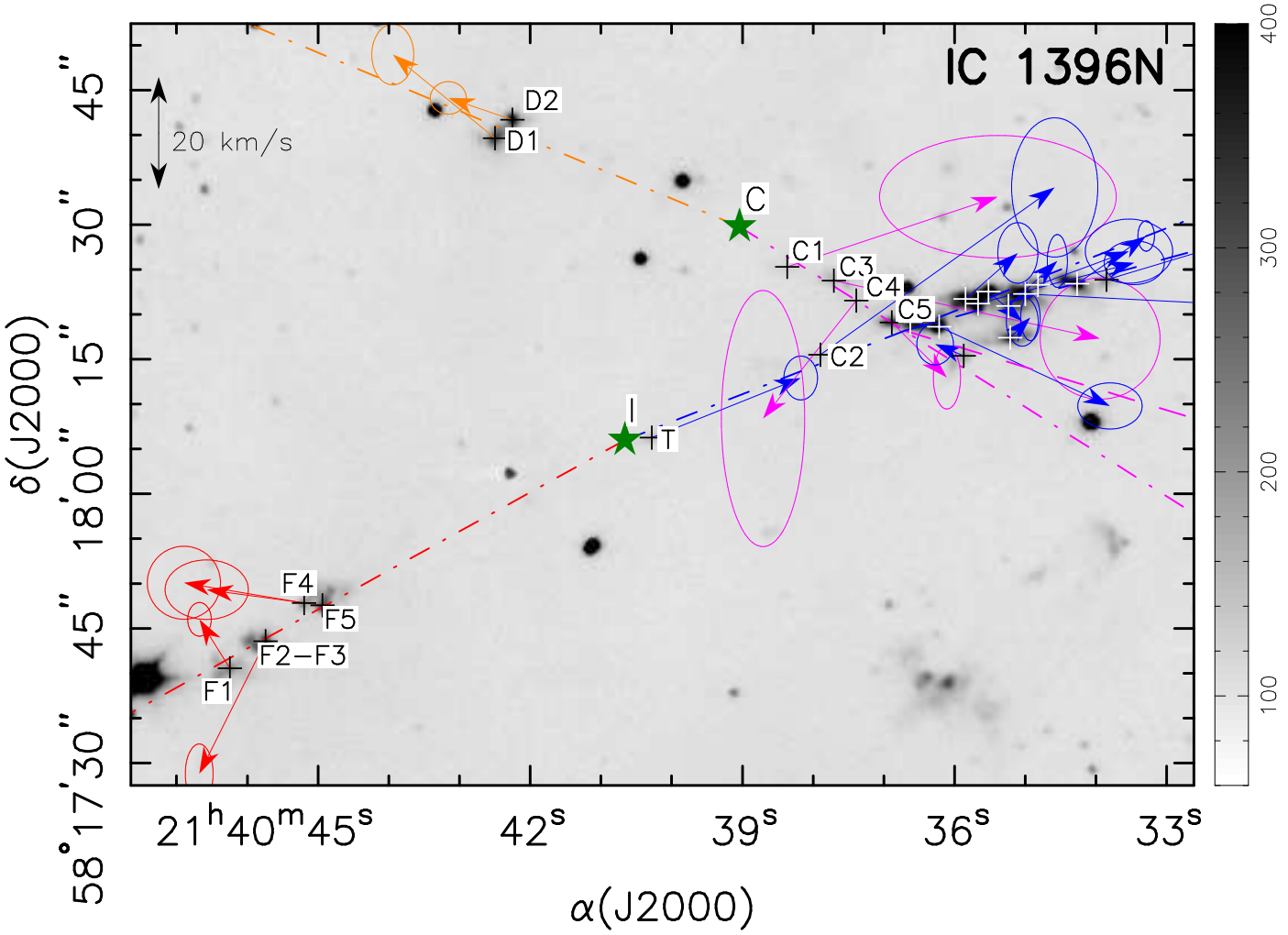

Fig. 3. Grey scale: first epoch H_2 image of IC 1396N obtained with the TNG, showing the positions and tangential velocity of the knots, derived from their proper motions, for a distance of 910 pc. The ellipses at the tip of each arrow indicate the uncertainty on the velocity. The axes of the red and blue lobes of outflow N are indicated respectively by the orange and magenta dash-dotted lines passing through the position of its exciting source, C. The axes of the red and blue lobes of outflow S are indicated respectively by the red and blue dash-dotted lines passing through the position of its exciting source, I. The large green star symbols mark the positions of the exciting sources C and I. The small black or white plus symbols mark the positions of the knots. An enlarged view of the interaction area can be seen in Fig. 4, where the identification of knots C6 to C17 is also shown.

Fig. 1). We determined the direction of the E and W lobes separately, allowing for a bending of the outflow at the position of the driving source C. We fitted two half lines with origin at the position of the driving source, minimising the sum of the squares of the distances to the half line of the positions of knots D1 and D2 and of the positions of C1, C3, C4, and C5. The results are shown in Table 2. As can be seen, the axes of the two lobes of outflow N have PAs that do not differ exactly at 180 degrees, but are bent with an angle of $9\overset{\circ}{.}8 \pm 0\overset{\circ}{.}6$ at the position of the driving source C.

The powering source of outflow S is source I, with coordinates $\alpha(J2000) = 21^{\rm h}40^{\rm m}40\overset{\rm s}{.}66$, $\delta(J2000) = +58°18'06\overset{''}{.}0$. The knots F1, F2-F3, F4, and F5 are moving eastward (CO red lobe), and T and C2 westward (CO blue lobe), toward the area of interaction (see Fig. 1).

We fitted two half lines with origin at the position of the source I to the positions of knots F1, F2-F3, F4, and F5, and knots T and C2, obtaining the results shown in Table 2. As can be seen, the axes of the two lobes of outflow S are bent with an angle of $5\overset{\circ}{.}6 \pm 0\overset{\circ}{.}3$ at the position of the driving source I. Both outflows N and S are bent at their driving source with a concavity pointing roughly southward.

The outflow axes are also traced by the high-velocity CO line observed by Beltrán et al. (2012). However, the CO is extended, the axes of the lobes can only be determined reliably where it is more collimated, close to the exciting sources, and the uncertainty on the direction of the axes from the CO is higher than that obtained for H_2 knot positions. We therefore used the latter to estimate the collision point (see following section).

3.2.2. Collision point

The (possible) collision point of the two outflows lies at the intersection of the N-blue and S-blue lobes. The direction of the S-blue axis is determined from the position of the driving source and only two knots, making its value less reliable than that of the N-blue axis. Depending on the direction adopted for the S-blue axis, the collision point nearly coincides with knot C5, or is ∼1″ south of knot C6.

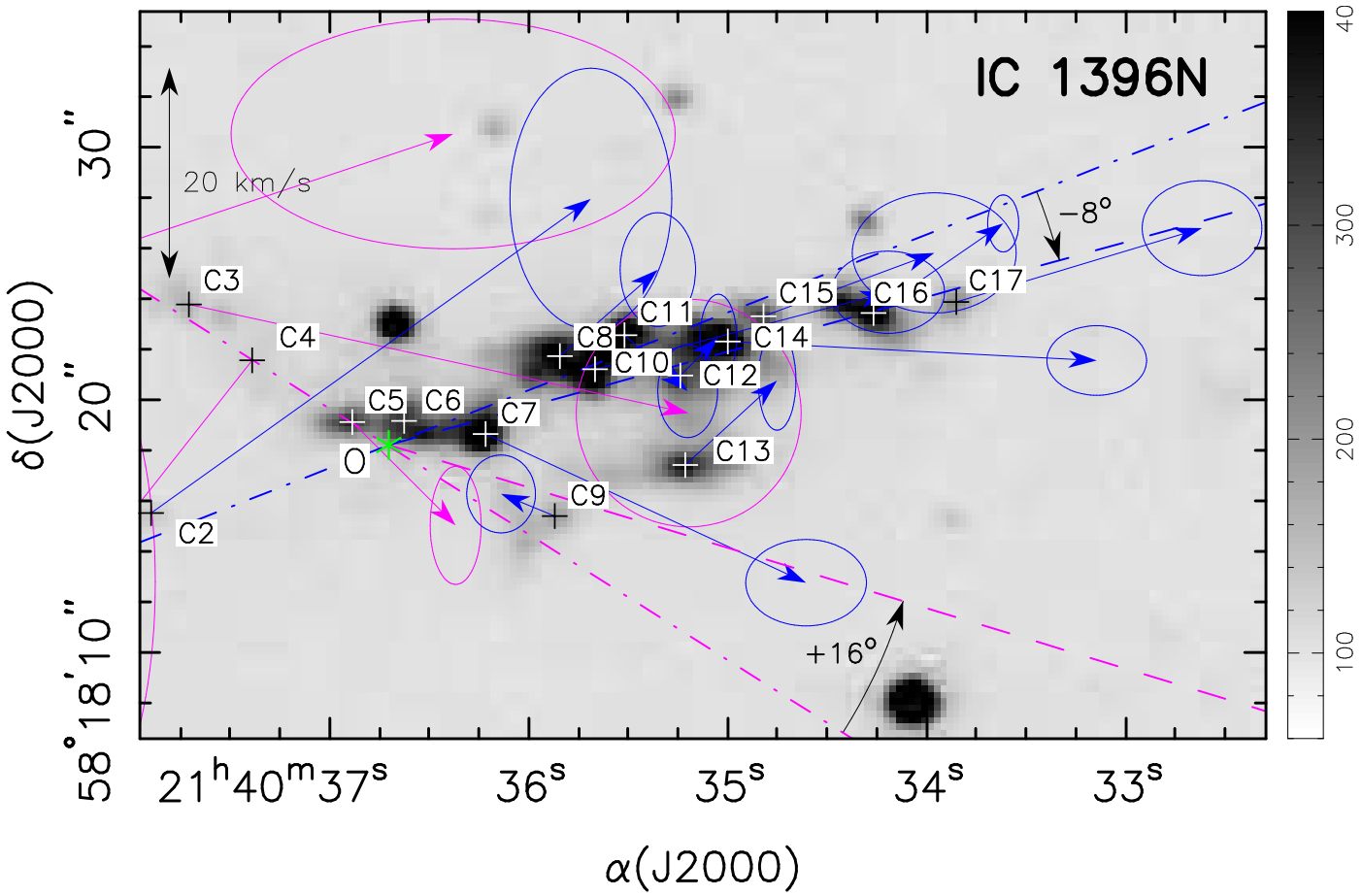

Fig. 4. Zoomed-in view of Fig. 3, showing the knots in the area of interaction between the two outflows and their proper motions. The blue-lobe pre-collision axes of outflows N and S are indicated respectively by the magenta and blue dash-dotted lines. Their intersection, the collision point O, is marked with a green asterisk. The dashed lines show the post-collision axes of outflow N (magenta) and outflow S (blue) (see Table 3).

Table 2. Pre-collision outflows axes passing through the position of each exciting source.

Outflow	Mean v_t [a] (km s^{-1})	Driving source	Lobe	Axis PA [b] (deg)	Bending [c] (deg)	$\langle d^2 \rangle^{1/2}$ [d] (arcsec)	Knots used
N	19.2 ± 4.1	C	Red	67.6 ± 0.3		1.3	D1, D2
			Blue	−122.3 ± 0.5	9.8 ± 0.6	0.5	C1, C3, C4, C5
S	20.5 ± 2.2	I	Red	118.9 ± 0.2		0.9	F1, F2-3, F4, F5
			Blue	−66.7 ± 0.3	5.6 ± 0.3	0.7	T, C2

Notes. [a]Scalar average of tangential velocities v_t. [b]PA of the best-fit half-line with origin at the corresponding exciting source. [c]Difference in direction between the blue and red lobes. [d]Root-mean-square distance of the knots to the axis (see Table A.2).

Interestingly, both knots show evidence of the interaction of the two outflows. On the one hand, the photometric data show that C5 is the only knot that shows variability between the three epochs, and is the knot with the highest increase in brightness (see Table A.1). On the other hand, knot C6 is the only knot that dramatically changes its morphology between the two epochs observed, as can be seen in Fig. 2. This suggests that these changes are possibly a consequence of the interaction of the two outflows and that knots C5 and C6 are most probably the closest knots to the collision point.

The size of the collision region, taken as the separation of knots C5 and C6, is of the order of 5000 au. We adopted a point of the N-blue axis close to the midpoint between knots C5 and C6 as the possible collision point. This point has coordinates $\alpha(J2000) = 21^h40^m36\overset{s}{.}71$, $\delta(J2000) = +58°18'18\overset{''}{.}1$. By adopting this collision point, knot C5 has to be considered as a pre-collision knot, and knots C6 to C17 as post-collision knots. The classification of knot C5 as pre-collision or post-collision is not critical for any of the results of this work.

3.2.3. Post-collision knots

As can be seen in Figs. 3 and 4, all the post-collision knots are located between the blue lobe axes of outflow N and outflow S. The knots C6, C7, and C9 are aligned near the blue lobe axis of outflow N, and because of this we identify them as belonging to outflow N. The rest of post-collision knots, namely C8 and C10 to C17, are clearly located to the south of the blue lobe axis of

Table 3. Post-collision outflows axes passing through the collision point, $\alpha(J2000) = 21^h40^m36\overset{s}{.}71$, $\delta(J2000) = +58°18'18\overset{''}{.}1$.

Outflow	Mean v_t [a] (km s^{-1})	Axis PA [b] (deg)	Deflection [c] (deg)	$\langle d^2\rangle^{1/2}$ [d] (arcsec)	Knots used
N	12.7 ± 5.1	-106.7 ± 0.8	15.6 ± 1.0	1.2	C6 [e], C7, C9
S	12.9 ± 1.7	-74.7 ± 0.2	-8.0 ± 0.3	1.6	C8, C10-17

Notes. [a]Scalar average of tangential velocity v_t. [b]PA of the best-fit half-line with origin at the position of the collision point. [c]Difference in PA between the post-collision axis and the pre-collision axis of the blue lobe from Table 2. [d]Root-mean square distance of the knots to the axis (see Table A.3). [e]For knot C6, only its position is used.

Table 4. Vectorial average of the tangential velocities of the pre-collision and post-collision knots of outflows N and S, and deviation $\langle\Delta PA\rangle$ from the corresponding outflow-lobe axis.

Ident. [b]	Axis PA [a] (deg)	$\langle v_x\rangle$ (km s^{-1})	$\langle v_y\rangle$ (km s^{-1})	$\langle PA\rangle$ (deg)	$\langle\Delta PA\rangle$ (deg)	Knots
N-red	67.6 ± 0.3	-14.3 ± 4.6	6.4 ± 2.6	65.9 ± 11.1	-1.7 ± 11.1	D1, D2
N-blue	-122.3 ± 0.5	9.4 ± 4.2	-6.7 ± 4.4	-125.6 ± 21.7	-3.3 ± 21.7	C1, C3, C4, C5
S-red	118.9 ± 0.2	-9.3 ± 2.9	1.3 ± 2.2	81.8 ± 13.6	-37.1 ± 13.6	F1, F2-3, F4, F5
S-blue	-66.7 ± 0.3	28.5 ± 5.3	12.3 ± 3.7	-66.6 ± 7.4	0.1 ± 7.4	T, C2
N-post	-106.7 ± 0.8	3.5 ± 5.4	-5.2 ± 2.8	-145.9 ± 42.6	-39.2 ± 42.6	C6, C7, C9
S-post	-74.7 ± 0.8	10.1 ± 1.6	4.6 ± 1.3	-65.8 ± 7.1	8.9 ± 7.1	C8, C10-17

Notes. [a]From Table 2. [b]Identification of the knot: outflow (N or S), and lobe, red, blue, or post-collision.

outflow S, but aligned roughly in the same direction, and because of this we identify them as belonging to outflow S.

In order to characterise the alignment of the post-collision knots, we fitted a half line with origin at the position of the collision point, minimising the sum of the squares of the distances to the line of the positions of the post-collision knots of outflow N and of the post-collision knots of outflow S. The results are shown in Table 3. As can be seen, the two groups of post-collision knots are well aligned with their axes, with average distances of $\sim 1''$, close to the values for the pre-collision knots (Table 2).

The change in direction of outflow N at the collision is of $+15\overset{°}{.}6 \pm 1\overset{°}{.}0$ (counterclockwise, northward), while that of outflow S is $-8\overset{°}{.}0 \pm 0\overset{°}{.}3$ (clockwise, southward). This change in direction of the post-collision knots of both outflows is a clear indication that there is an interaction between the two outflows, giving support to the scenario of collision, where the knots of outflow N are pushed northward, and the knots of outflow S are pushed southward from their original pre-collision direction.

3.3. Proper motion directions with respect to the outflow axis

Let us compare the direction of the tangential velocity of the knots with the directions of the outflow lobes previously derived. For this, we calculated the direction of the average tangential velocity of the pre-collision knots of the E lobe of outflows N and S, and pre-collision and post-collision knots of the W lobe of outflows N and S. The average was obtained taking into account the error in each value of the tangential velocities. The results obtained are shown in Table 4.

For the pre-collision knots, we can see that the deviation of the direction of the tangential velocity with respect to their respective axes has a large dispersion, but with an average value compatible with zero. For the post-collision knots, the uncertainty on their average PA is so large that the result is inconclusive, although their average PA is compatible with that of the pre-collision knots.

Table 5. Average deviation of the tangential velocity of the post-collision knots from the radial direction from the collision point, $\alpha(J2000) = 21^h40^m36\overset{s}{.}71$, $\delta(J2000) = +58°18'11\overset{''}{.}1$ (see Table A.4).

Ident.	Mean ΔPA (deg)	rms (deg)	Knots
N-post	-20.5 ± 9.8	48.4	C7, C9
S-post	-5.8 ± 3.8	21.2	C8, C10-17
(N+S)-post	-7.8 ± 3.6	26.4	C7-17

3.4. Deviation with respect to the radial direction from the collision point

Let us analyse whether the tangential velocities of the post-collision knots are distributed radially from the collision point. Firstly, if we assume that the post-collision knots are ballistic, the quadratic average distance of their trajectories to the collision point should be small. Its value is $\langle d^2\rangle^{1/2} = 5\overset{''}{.}4$ (see Table A.5) and therefore the result is inconclusive. Secondly, we computed the difference between the tangential velocity PA and the radial direction from the collision point. The results are shown in Table 5. The average value of the angle difference is small, $-7\overset{°}{.}8 \pm 3\overset{°}{.}6$, but the dispersion is high, 26°. Although the dispersion of the direction of the proper motions is high, they are on average radially distributed from the collision point. Thus, the distribution of the tangential velocities of the post collision knots is consistent with the scenario of a collision of the two outflows at the collision point.

3.5. Full spatial velocities

Table 1 displays the full velocity, v_{tot}, for the knots for which the radial velocity, v_r, was derived from the H_2 $\upsilon = 1$–0 S(1) spectra of Massi et al. (2022). In addition, we derived the inclination

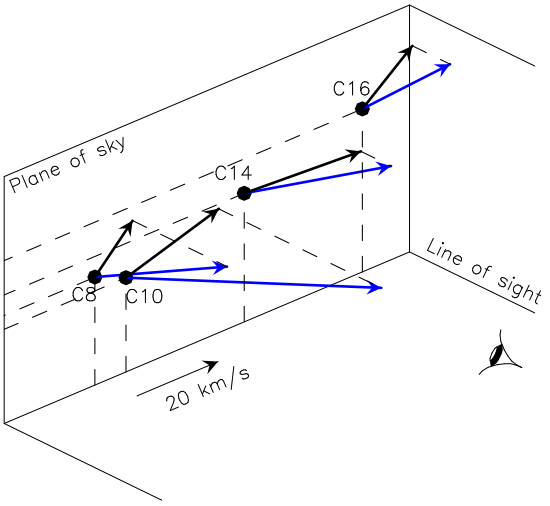

Fig. 5. Sketch of the 3D velocities of the post-collision knots C8, C10, C14, and C16 of outflow S. The black arrows are velocities in the plane of the sky derived from the proper motions. The blue arrows are the 3D velocities, with a radial component towards the observer.

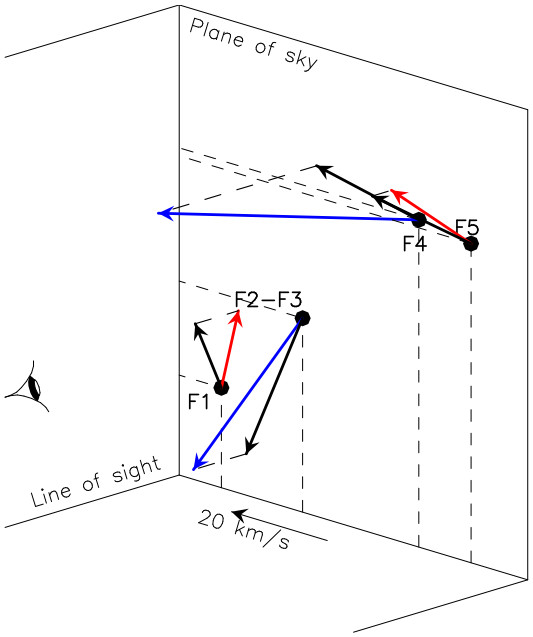

Fig. 6. Sketch of the 3D velocities of the pre-collision knots F1, F2-3, F4, and F5 of the eastern lobe of outflow S. The black arrows are velocities in the plane of the sky derived from the proper motions. The blue and red arrows are the 3D velocities, with a radial component toward and away from the observer, respectively.

angle, i, between the knot motion and the plane of the sky (with $i > 0$ away from the observer). For the rest of the knots, only the tangential velocity, v_t, was obtained from the proper motion.

Unfortunately the radial velocities of all the F, D, and C knots of the H_2 outflows could not be obtained because the long-slit positions did not encompass all of their emission. The C knots with observed radial velocity (C8, C10, C14, C16) have blueshifted velocities ranging from approximately −10 to −50 km s^{-1} (see Fig. 5). Their radial velocity is fully compatible with belonging to the blueshifted lobe of the CO outflow. Regarding the F knots (F1, F2-3, F4, F5), CO(1–0) emission (see Fig. 1) indicates that knots F should be redshifted. Knots F1 and F5 are consistent with the CO data. However, F2 and F4 are clearly blueshifted (−10 to approximately −30 km s^{-1}) (see Fig. 6). This may suggest that the F knots are tracing a bow shock with its axis near the plane of the sky, with knots F2, F3, and F4 in the foreground, and knots F1 and F5 in the background (Massi et al. 2022).

4. Discussion

The position and proper motions of the knots that are far from the interaction area are consistent with D1 and D2 belonging to the N-red lobe, and C1, C3, C4, and C5 belonging to the N-blue lobe of outflow N; F1, F2-3, F4, and F5 belonging to the S-red lobe; and T and C2 to the S-blue lobe of outflow S. The positions of these knots were used to derive the direction of the axes of the outflow lobes. Both outflow N and outflow S are slightly bent at the position of their respective exciting sources. The difference in PA of the red and blue lobes of outflow N is $9\overset{\circ}{.}8 \pm 0\overset{\circ}{.}6$. For outflow S, the difference in PA is $5\overset{\circ}{.}6 \pm 0\overset{\circ}{.}3$. For both outflows, the bending at the position of the exciting source produces a concavity pointing roughly southward.

The intersection of the blue lobes of outflows N and S has been identified as the (possible) collision point, O. The area of (possible) interaction between the two outflows is westward of the collision point. The position and proper motion of the knots in the area of interaction has made it possible to identify the knots of the blue lobes of both outflows (which we refer to as post-collision knots) as belonging to outflow N (N-post), namely C6, C7, and C9; or belonging to outflow S (S-post), namely C8 and C10 to C17.

Both the N-post and S-post knots are well aligned along an axis passing through the collision point, which is bent with respect to the axis of the corresponding blue lobe. For outflow N, the axis of the post-collision knots deviates $+15\overset{\circ}{.}6 \pm 1\overset{\circ}{.}0$ (counterclockwise, northward) from its original pre-collision direction. For outflow S, the deviation of the axis of the post-collision knots from its original pre-collision direction is $-8\overset{\circ}{.}0 \pm 0\overset{\circ}{.}3$ (clockwise, southward). This is consistent with the collision scenario, with the N-post knots being pushed northward by outflow S coming from the south, and the S-post knots being pushed southward by outflow N coming from the north. The deviation angle is of the same order for both outflows, as would be expected for two outflows with a similar linear momentum (Beltrán et al. 2012), and confirmed by the similar value of the average tangential velocity of the pre-collision knots (Table 2). However, the deviation angles are small, indicating that the interaction between the two outflows is most probably not a head-on collision, but a grazing collision.

The values of the linear momentum of the CO outflows reported by Beltrán et al. (2012) are 0.06 $M_\odot$ km s^{-1} for the blue lobe of outflow N and 0.09 $M_\odot$ km s^{-1} for the blue lobe of outflow S. The deviation of $15\overset{\circ}{.}6$ of the blue lobe of outflow N requires a change in its linear momentum of 0.017 $M_\odot$ km s^{-1}, which is 19% of the linear momentum of the blue lobe of outflow S. Similarly, the deviation of $8\overset{\circ}{.}0$ of the blue lobe of outflow S requires a change in linear momentum of 0.013 $M_\odot$ km s^{-1}, which is 21% of the linear momentum of the blue lobe of outflow S. These figures are consistent with a scenario of a collision of both outflows, with an interchange of the same amount of linear momentum, ∼0.015 $M_\odot$ km s^{-1}, which is a fraction of ∼20% of their pre-collision linear momentum.

The proper motion of the post-collision knots is consistent with their tangential velocities being radial with respect to the

collision point, with an average difference in direction from radial of $\Delta PA = -8° \pm 4°$; but the rms dispersion is high, $\sigma_{\Delta PA} = 26°$. The 3D velocity of a few of the knots was obtained using the line-of sight velocities obtained by Massi et al. (2022). The radial velocity of the C knots is fully compatible with belonging to the blueshifted lobe of the CO outflow. Regarding the F knots, their 3D velocity suggests that they could be tracing a bow shock with its axis near the plane of the sky (Massi et al. 2022).

5. Conclusions

There is strong evidence of interaction of the N and S outflows of IC 1396N. On the one hand, there is a clear enhancement of shock-excited H_2 emission in the region of interaction. On the other hand, the deviations of the post-collision axes are consistent with an interchange of a similar amount of linear momentum between the two outflows, with the collision point located near the C5 and C6 knots. The location of the collision point is based on the fact that C5 is the knot that shows the highest variability between the three epochs, and C6 is the only knot with a significant change of morphology. Thus, they are most probably the closest knots to the collision point. In addition, the motion of the post-collision knots is consistent with radial motion from the collision point. The small deviation of the post-collision knots implies that the interaction is not a head-on collision, but likely a grazing collision.

Additional observations would help to confirm the collision scenario. In particular, a third epoch H_2 image with a time interval of ∼10 yr (that is, around 2027) would allow us to discriminate proper motions from changes in morphology of the knots. In addition, integral field spectroscopy of the region of interaction would be necessary in order to obtain accurate measurements of the radial velocities of more than a few knots.

Acknowledgements. We thank the referee for his/her helpful comments. This work has been partially supported by the Spanish MINECO grants AYA2014-57369-C3 and AYA2017-84390-C2 (cofunded with FEDER funds), the PID2020-117710GB-I00 grant funded by MCIN/ AEI /10.13039/501100011033, and the MDM-2014-0369 of ICCUB (Unidad de Excelencia 'María de Maeztu'), and by the program Unidad de Exceencia 'María de Maeztu' CEX2020-001058-M.

References

Acosta Pulido, J. A., Ballesteros, E., Barreto, M., et al. 2003, The Newsletter of the Isaac Newton Group of Telescopes, 7, 15
Anglada, G., López, R., Estalella, R., et al. 2007, AJ, 132, 2799
Beltrán, M. T., Massi, López, R., Girart, J.M., & Estalella, R. 2009, A&A, 504, 97
Beltrán, M. T., Massi, F., Fontani, F., Codella, C., & López, R. 2012, A&A, 542, L26
Caratti o Garatti, A., Giannini, T., Nisini, B., & Lorenzetti, D. 2006, A&A, 449, 1077
Manchado, A., Barreto, M., Acosta-Pulido, J., et al. 2004, SPIE, 5492, 1094M
Massi, F., López, R., Beltrán, M. T., Estalella, R., & Girart, J. M. 2022, A&A, submitted
Sugitani, K., Fukui, Y., & Ogura, K. 1991, ApJS, 77, 59
Zapata, L. A., Fernández-López, M., Rodríguez, L. F., et al. 2018, AJ, 156, 239
Zucker, C., Speagle, J. S., Schlafly, E. F., et al. 2020, A&A, 633, A51

Appendix A: Photometry of the knots and additional tables

Table A.1 shows the differential photometry of the knots of the IC 1396N outflows of two previous images taken in 2003 (Caratti o Garatti et al. 2006) and 2005 (Beltrán et al. 2009) with respect to the image obtained in the present work. The rest of tables show the values for each knot used for computing the average values of distances to the outflow axes (Tables A.2 and A.3), radial PA from the collision point (Table A.4), and distances of the ballistic trajectories to the collision point (Table A.5).

Table A.1. Differential photometry of the knots ofIC 1396N: difference in magnitude from the 2003 and 2005 images to the 2016 image of this work.

Knot	Epoch 2003[a] (mag.)	Epoch 2005[b] (mag.)
C1	-0.20 ± 0.11	$+0.02 \pm 0.08$
C2	-0.11 ± 0.09	-0.02 ± 0.07
C3	-0.31 ± 0.07	$+0.04 \pm 0.04$
C4	-0.18 ± 0.07	$+0.07 \pm 0.05$
C5	-0.42 ± 0.03	-0.15 ± 0.02
C6	-0.08 ± 0.01	$+0.05 \pm 0.01$
C7	-0.03 ± 0.01	$+0.10 \pm 0.01$
C8	$+0.07 \pm 0.01$	$+0.14 \pm 0.01$
C9	-0.18 ± 0.03	-0.05 ± 0.03
C10	-0.21 ± 0.01	$+0.05 \pm 0.01$
C11	-0.00 ± 0.01	-0.01 ± 0.01
C12	-0.04 ± 0.02	$+0.03 \pm 0.01$
C13	-0.08 ± 0.01	-0.03 ± 0.01
C14	$+0.04 \pm 0.01$	$+0.06 \pm 0.01$
C15	$+0.15 \pm 0.02$	-0.04 ± 0.02
C16	$+0.02 \pm 0.01$	$+0.04 \pm 0.01$
C17	$+0.01 \pm 0.03$	-0.14 ± 0.03
D1	-0.01 ± 0.02	-0.01 ± 0.01
D2	-0.14 ± 0.02	-0.00 ± 0.02
F1	$+0.01 \pm 0.02$	$+0.21 \pm 0.02$
F2	$+0.02 \pm 0.02$	$+0.04 \pm 0.02$
F3	-0.32 ± 0.03	-0.00 ± 0.02
F4	-0.07 ± 0.05	$+0.05 \pm 0.04$
F5	$+0.02 \pm 0.02$	$+0.09 \pm 0.02$
T	-0.36 ± 0.14	-0.06 ± 0.09

Notes. [(a)]From the image of Caratti o Garatti et al. (2006) [(a)]From the image of Beltrán et al. (2009)

Table A.2. Distance of the pre-collision knots to the outflow axes, passing through the exciting sources C (outflow N) and I (outflow S) (see Table 2).

Knot	Axis	d (arcsec)
D1	N-red	1.29
D2	N-red	1.34
	$\langle d^2 \rangle^{1/2}$ =	1.32
C1	N-blue	0.96
C3	N-blue	0.52
C4	N-blue	0.02
C5	N-blue	0.03
	$\langle d^2 \rangle^{1/2}$ =	0.55
F1	S-red	0.98
F2-F3	S-red	0.26
F4	S-red	1.38
F5	S-red	0.16
	$\langle d^2 \rangle^{1/2}$ =	0.86
T	S-blue	0.92
C2	S-blue	0.11
	$\langle d^2 \rangle^{1/2}$ =	0.66

Table A.3. Distance of the post-collision knots to the outflow post-collision axes passing through the collision point, $\alpha(J2000) = 21^h40^m36\overset{s}{.}71$, $\delta(J2000) = +58°18'18\overset{''}{.}1$, and with PAs $-106\overset{°}{.}7$ (outflow N) and $-74\overset{°}{.}7$ (outflow S) (see Table 3).

Knot	Axis	d (arcsec)
C6	N-post	1.09
C7	N-post	1.52
C9	N-post	0.81
	$\langle d^2 \rangle^{1/2}$ =	1.18
C8	S-post	1.61
C10	S-post	0.75
C11	S-post	1.74
C12	S-post	0.38
C13	S-post	3.85
C14	S-post	0.42
C15	S-post	1.02
C16	S-post	0.01
C17	S-post	0.45
	$\langle d^2 \rangle^{1/2}$ =	1.58

Table A.4. Radial PA from the collision point to the post-collision knots position, and deviation from their tangential velocity PA, ΔPA. The collision point considered is $\alpha(J2000) = 21^h40^m36\overset{s}{.}71$, $\delta(J2000) = +58°18'18\overset{''}{.}1$ (see Table 5).

Knot	Radial PA (deg)	ΔPA (deg)
C7	−84	−31 ± 10
C9	−113	180 ± 43
C8	−117	69 ± 28
C10	−70	−6 ± 9
C11	−65	−66 ± 35
C12	−77	32 ± 42
C13	−94	46 ± 20
C14	−73	−20 ± 5
C15	−71	1 ± 25
C16	−75	19 ± 10
C17	−76	3 ± 13
	$\langle\Delta PA\rangle$ =	−7.8 ± 3.6
	$\sigma_{\Delta PA}$ =	26.4

Table A.5. Distances of the ballistic trajectories of the post-collision knots to the collision point, $\alpha(J2000) = 21^h40^m36\overset{s}{.}71$, $\delta(J2000) = +58°18'18\overset{''}{.}1$.

Knot	d (arcsec)
C7	2.0
C9	0.1
C8	1.9
C10	0.8
C11	9.4
C12	6.2
C13	8.5
C14	4.8
C15	0.4
C16	6.6
C17	1.0
$\langle d^2\rangle^{1/2}$ =	5.0